Hindawi
Wireless Communications and Mobile Computing
Volume 2018, Article ID 9783863, 12 pages
https://doi.org/10.1155/2018/9783863

Research Article

Predicting Wireless MmWave Massive MIMO Channel Characteristics Using Machine Learning Algorithms

Lu Bai,[1] Cheng-Xiang Wang,[2] Jie Huang,[1] Qian Xu,[3] Yuqian Yang,[1] George Goussetis,[2] Jian Sun,[1] and Wensheng Zhang[1]

[1]*Shandong Provincial Key Lab of Wireless Communication Technologies, School of Information Science and Engineering, Shandong University, Qingdao, Shandong 266237, China*
[2]*Institute of Sensors, Signals and Systems, School of Engineering and Physical Sciences, Heriot-Watt University, Edinburgh EH14 4AS, UK*
[3]*School of Computer Science and Technology, Jilin University, Changchun, Jilin 130012, China*

Correspondence should be addressed to Cheng-Xiang Wang; cheng-xiang.wang@hw.ac.uk

Received 31 March 2018; Accepted 16 July 2018; Published 23 August 2018

Academic Editor: Tommi Jamsa

Copyright © 2018 Lu Bai et al. This is an open access article distributed under the Creative Commons Attribution License, which permits unrestricted use, distribution, and reproduction in any medium, provided the original work is properly cited.

This paper proposes a procedure of predicting channel characteristics based on a well-known machine learning (ML) algorithm and convolutional neural network (CNN), for three-dimensional (3D) millimetre wave (mmWave) massive multiple-input multiple-output (MIMO) indoor channels. The channel parameters, such as amplitude, delay, azimuth angle of departure (AAoD), elevation angle of departure (EAoD), azimuth angle of arrival (AAoA), and elevation angle of arrival (EAoA), are generated by a ray tracing software. After the data preprocessing, we can obtain the channel statistical characteristics (including expectations and spreads of the above-mentioned parameters) to train the CNN. The channel statistical characteristics of any subchannels in a specified indoor scenario can be predicted when the location information of the transmitter (Tx) antenna and receiver (Rx) antenna is input into the CNN trained by limited data. The predicted channel statistical characteristics can well fit the real channel statistical characteristics. The probability density functions (PDFs) of error square and root mean square errors (RMSEs) of channel statistical characteristics are also analyzed.

1. Introduction

The fifth generation (5G) wireless communication networks have lots of novel requirements, such as the 1000 times the system capacity with respect to the fourth generation (4G) networks, wide frequency range (covering millimetre wave (mmWave) bands, e.g., 450 MHz–100 GHz), increased data rate, reduced latency, energy, and cost [1–6]. To satisfy the above-mentioned requirements, several advanced technologies, such as mmWave and massive multiple-input multiple-output (MIMO), have been proposed and brought new challenges on channel modeling. Since the performance bound of wireless communication systems is determined by channel characteristics [7], an accurate channel model plays an important role in designing, evaluating, and developing wireless communication systems. The 5G wireless communication channel models, such as mobile and wireless communications Enablers for the Twenty-twenty Information Society (METIS) channel model [8], Millimetre-Wave Evolution for Backhaul and Access (MiWEBA) channel model [9], ITU-R IMT-2020 channel model [10], COST 2100 channel model [11, 12], IEEE 802.11 ay channel models [13], millimetre-wave based mobile radio access network for fifth generation integrated communications (mmMAGIC) channel model [14], quasi deterministic radio channel generator user manual and documentation (QuaDRiGa) channel model [15, 16], and a general three-dimensional (3D) nonstationary 5G channel model [17], can be classified as deterministic and stochastic channel models. As the most important technologies of 5G wireless communication networks, massive MIMO and mmWave have also attracted great attentions. According to the massive MIMO and mmWave indoor channel measurement in [18], authors in [19] did the massive MIMO and mmWave channel parameter estimation.

Authors in [20] summarized recent massive MIMO channel measurements and models. The above-mentioned models are complex and hard to use. So a revolutionary channel model is necessary.

The explosive increase of frequencies/bandwidths, antennas, and new services/scenarios will generate massive data and bring the research of 5G wireless communications to the era of artificial intelligence (AI) [21, 22]. Machine learning (ML), as an important branch of AI, has received extensive attentions due to its capability of digging the valuable and hidden rules from enormous unknown channel information. It can take advantages of both the low complexity of stochastic channel models and the accuracy of deterministic channel models. As a conventional ML algorithm, convolutional neural network (CNN) exhibits excellent performance on compressing and processing redundant channel information [23].

Until now, there are two kinds of applications of AI to 5G wireless communication channels. One is measurement data preprocessing based on statistical learning methods, e.g., clustering algorithms. The Kernel-Power-Density algorithm proposed in [24] used the kernel density and only considered the neighboring points when computing the density. Authors in [25] proposed a novel clustering framework based on Kernel-Power-Density algorithm and took elevation angles into consideration. The Kuhn–Munkres algorithm was proposed to solve the tracking problem in [26]. The Kalman filter in [27] was used to track the clusters and to predict the cluster positions. Furthermore, several other algorithms were used for clusters identification in measurement data preprocessing, such as KPowerMeans algorithm [28] and hierarchical tree [29]. The above-mentioned clustering algorithms play a significant role in conventional cluster-based stochastic channel models, such as COST 2100 channel model and WINNER channel models, but it cannot predict the channel characteristics. The other one is to predict the channel characteristics based on ML algorithms which can dig the mapping relationship between physical environment information and the channel characteristics. The function between frequency, distance, and path loss (PL) was modeled by two types of artificial neural networks (ANNs), i.e., multilayer perceptron (MLP) and radial basis function (RBF) [30–34]. In [35], PL was also modeled as a mapping relationship between delay and the atmosphere by MLP. Authors in [36] and [37] modeled Doppler frequency shift by RBF and MLP, respectively. The mapping relationship between channel characteristics and geographical location was modeled by a feed-forward network (FFN) in [38] and a DeepFi architecture in [39]. In-vehicle wireless channels at 60 GHz were modeled by a FFN and a RBF network [40, 41]. Author in [42] proposed a three-layer structure based on ML –"wave, cluster-nuclei, and channel". Most of the existing research works can only obtain the mapping relationship between a single channel characteristic and physical channel environment information but cannot predict comprehensive channel characteristics. At the same time, the channel characteristics of any subchannels in a specified scenario cannot be predicted until now, while they play an important role on channel estimation and communication quality. CNN can compress and process redundant channel information well, but it has not been applied to channel characteristics prediction.

In this paper, we propose an AI enabled procedure to predict channel statistical characteristics based on CNN to obtain the mapping relationship between the location information of transmitter (Tx) and receiver (Rx) antennas and almost all the characteristics of amplitude, delay, and angles. The main **contributions** of this paper are summarized as follows:

(1) A procedure of predicting channel statistical characteristics based on a specified CNN for 3D mmWave MIMO indoor channels is proposed in this paper. With the location information of Tx and Rx antennas, the CNN can predict eleven comprehensive channel statistical characteristics, including PL, delay spread (DS), delay mean (DM), azimuth angle mean of departure (AAMD), azimuth angle mean of arrival (AAMA), azimuth angle spread of departure (AASD), azimuth angle spread of arrival (AASA), elevation angle mean of departure (EAMD), elevation angle mean of arrival (EAMA), elevation angle spread of departure (EASD), and elevation angle spread of arrival (EASA).

(2) This is the first time to compare five different wireless channel characteristic datasets, which are collected by different ways. By comparing their training results, we can obtain better rules of data generation and collection. Therefore, it has a profound guiding significance for data generation and collection.

We have organized the rest of the paper as follows. The AI enabled procedure to predict channel statistical characteristics is shown in Section 2. In Section 3, we describe the two indoor scenarios of data collection and the principle of data preprocessing. The five datasets are also given in this section. The proposed CNN is shown in Section 4. In Section 5, we discuss and analyze the results. Conclusions and future work are given in Section 6.

2. System Model

The flowchart of AI enabled procedure to predict channel statistical characteristics is shown in Figure 1. Firstly, we set up the indoor scenario and obtain simulated channel information. At this time, we construct two 3D indoor scenarios by setting the sizes and materials of rooms and objects in a ray tracing software. Then we can obtain the multipath component parameters (amplitude, delay, azimuth angle of departure (AAoD), elevation angle of departure (EAoD), azimuth angle of arrival (AAoA), and elevation angle of arrival (EAoA)). We do the data preprocessing to obtain the channel statistical characteristics (PL, DM, DS, AAMA, AASA, AAMD, AASD, EAMA, EASA, EAMD, and EASD) to build the dataset. The dataset of the specified indoor scenario is built to be separated as two sets by the proportion of 7:3 randomly. One is the train set, the other is the validation set. Samples in both the train set and the validation set have 3D coordinates of Tx and Rx as

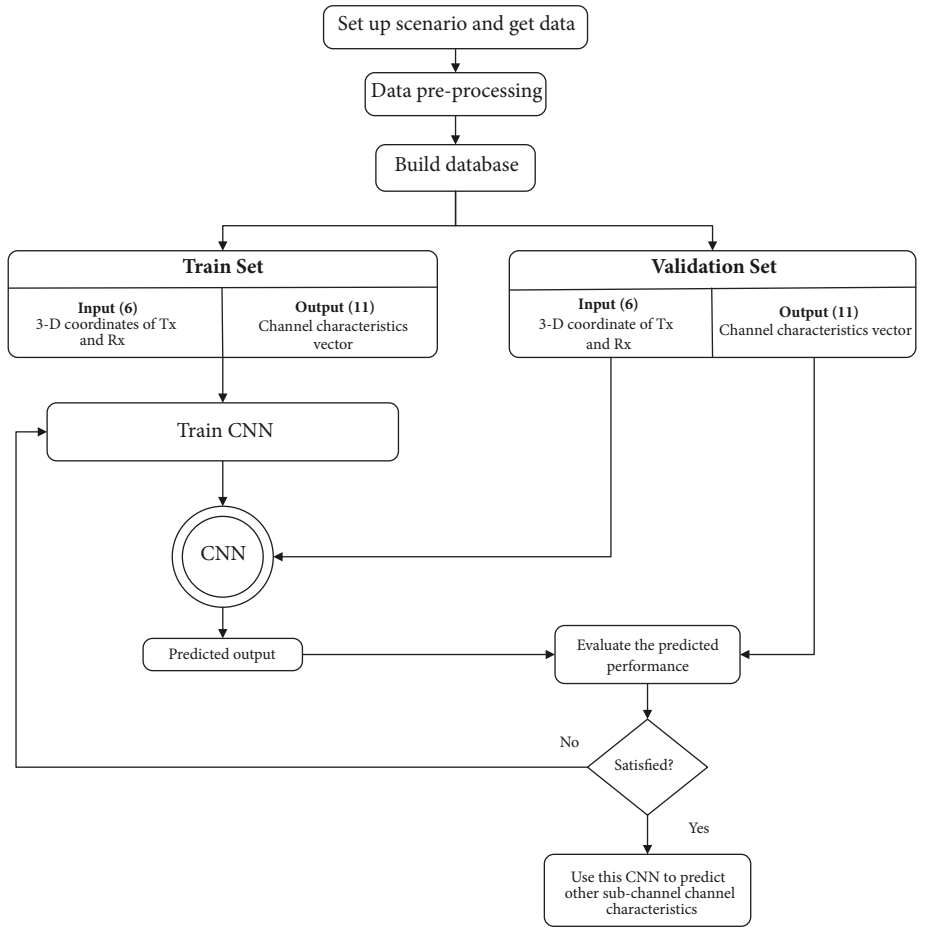

Figure 1: The flowchart of channel characteristic predicting procedure.

input vectors and channel statistical characteristics as output vectors. The train set is used to train the CNN. The input vectors of the validation set are put into the CNN to obtain the predicted output vectors. Whether train the CNN again or not is determined by comparing and analyzing the root mean square errors (RMSEs) and probability density functions (PDFs) between the predicted output vectors and output vectors of the validation set. More detailed information will be shown in the following sections.

3. Database Generation

The ray tracing software, Wireless InSite [43], is used to build the simulation datasets. Ray tracing is a classical deterministic method used for modeling radio propagations. It is based on the geometrical optic (GO) and uniform theory of diffraction (UTD). The interactions between rays and objects can be classified as reflection, transmission, scattering, and diffraction. By tracing paths in a specified scenario we build in the simulator, all the possible rays can be obtained and we can get the parameter vector $\omega_{ij,s}$ of the s-th ($s = 1, 2, \ldots, S$, $S = 250$) multipath between the i-th Tx antenna and j-th Rx antenna; i.e.,

$$\omega_{ij,s} = \left[\alpha_{ij,s}, \tau_{ij,s}, \theta^{\mathrm{T}}_{ij,s}, \phi^{\mathrm{T}}_{ij,s}, \theta^{\mathrm{R}}_{ij,s}, \phi^{\mathrm{R}}_{ij,s}\right] \quad (1)$$

where $\alpha_{ij,s}, \tau_{ij,s}, \theta^{\mathrm{T}}_{ij,s}, \phi^{\mathrm{T}}_{ij,s}, \theta^{\mathrm{R}}_{ij,s}$, and $\phi^{\mathrm{R}}_{ij,s}$ are the amplitude, delay, AAoD, EAoD, AAoA, and EAoA of the s-th multipath between the i-th Tx antenna and j-th Rx antenna, respectively.

3.1. The Descriptions of Data Generation. To verify the general predicted capability of the CNN, we construct two indoor scenarios in Wireless InSite to collect multipath component parameters. One is a virtual classroom scenario shown in Figure 2; the other is a real lab scenario shown in Figure 3.

3.1.1. The Virtual Classroom Scenario. The virtual classroom environment is about $8 \times 6 \times 3$ m^3 with 12 desks whose size is about $1.6 \times 0.4 \times 1.2$ m^3. The intervals of desks are 0.6 m along x-axis and 0.8 m along y-axis. Desks are made of wood. The ceiling is made of concrete. Both floor and walls are made of 3-layered dielectric in [44]. The layout of the classroom is shown in Figure 2(a). Figure 2(b) shows the 3D ray tracing scenario of the classroom constructed in Wireless InSite.

In this virtual scenario, at most 3 orders of reflection and 1 order of diffraction are simulated. The maximum number

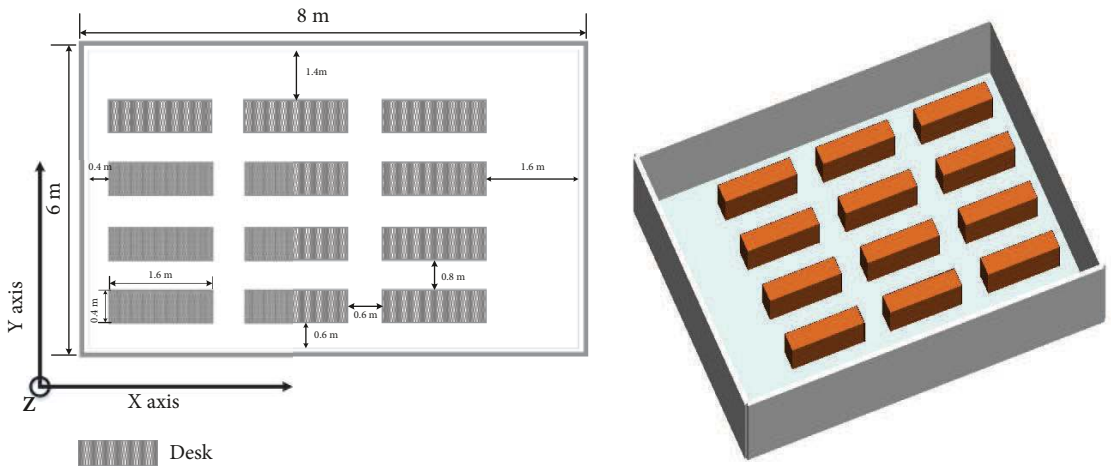

(a) The layout of the virtual scenario.

(b) The 3D ray tracing scenario of the virtual scenario.

Figure 2: The environment information of the virtual scenario.

of paths allowed in simulation is 250. For the complexity of simulation, we do not take scattering which is caused by surface roughness into consideration while the power loss caused by rough surface of objects is calculated by the reflection coefficient multiplied with roughness coefficient. The carrier frequency and bandwidth are set to 60 GHz and 2 GHz, respectively. To evaluate the performance of data collection, two datasets are built. In the 10 × 100 random dataset (10100R, R stands for random) of the virtual classroom scenario, we set up 10 Tx isotropic antennas with 0 dBi antenna gain in all directions and 100 Rx isotropic antennas at random location information to obtain multipath parameters of 1000 subchannels. 32 Tx isotropic antennas and 32 Rx isotropic antennas are randomly set up in 32 × 32 random dataset (3232R, R stands for random) of the virtual classroom scenario to obtain channel parameters of 1024 subchannels. In indoor uplink communication scenarios, the Txs can be mobile phones, laptops, iPads, etc., while the Rxs are normally access points (APs) located on the ceilings. In a virtual classroom environment, we assume that the height of Txs is 1.5 m and the height of Rxs is 3 m.

3.1.2. The Lab Scenario. The size of the lab scenario is approximately $7.2 \times 7.2 \times 2.7\ \mathrm{m}^3$. Its floor and ceiling are made of concrete but decorated with antistatic-electricity board. It has four sides of walls. One is a partition wall which is made of plaster board, and other sides of wall are made of concrete. Two high built small windows are on the one side wall while a large window almost cover the other side of wall. The lab is furnished with multiple desks and chairs, and other office furniture such as computers, bookshelf, and electronic devices. Desks made of frosted surface chipboard are about 0.75 m height at desktop level but with two or three additional 0.45 m clapboards. Chairs are made of fabric cover and metal and plastic support. The electromagnetic properties of above-mentioned building and furniture materials were characterized by a lot of material measurements [45–47]. There is a small storage room in the corner of the lab. The photo and layout of the lab are shown in Figures 3(a) and 3(b), respectively. Figure 3(c) shows the 3D ray tracing scenario of the lab constructed in Wireless InSite.

The lab supplies such as books and computer monitors on the desk are not modeled in the 3D ray tracing scenario, because their irregular shapes lead to significant increase of computational complexity and they are shadowed by higher clapboards on the desktop usually. Similarly, we also neglect chairs in the scenario modeling because they are about 0.8 m high which is lower than antennas and chairs were positioned nearby the desks. Since the lab scenario is more complex than the virtual classroom, at most 5 orders of reflection, 3 orders of transmission, and 1 order of diffraction are simulated in the ray tracing setup of this lab scenario. The maximum number of propagation paths is 250. The carrier frequency and bandwidth are set to 60 GHz and 2 GHz, respectively. To evaluate the performance of data collection, three datasets are built. In the 30 × 30 random dataset (3030R, R stands for random) of the lab scenario, we set up 30 Tx isotropic antennas and 30 Rx isotropic antennas at random location information to obtain channel parameters of 900 subchannels. 30 Tx isotropic antennas and 30 Rx isotropic antennas are set up by grid at 1 m intervals in 30 × 30 grid dataset (3030G, G stands for grid) of the lab scenario to obtain multipath component parameters of 900 subchannels. Similarly, 211 Tx isotropic antennas and 211 Rx isotropic antennas are set up by grid at 0.4 m intervals in the 211 × 211 grid dataset (211211G, G stands for grid) of the lab scenario to get channel parameters of 44521 subchannels. In the lab environment, we assume that the height of Txs is 1.5 m and the height of Rxs is 2.7 m.

3.2. Data Processing. For conciseness, we use channel characteristic vector ϖ_{ij} instead of the parameter vectors of 250 multipaths; i.e.,

$$\varpi_{ij} = \left[\rho_{ij}, \mu_{ij}, \mu_{\mathrm{M},ij}, \vartheta^{\mathrm{T}}_{ij}, \varphi^{\mathrm{T}}_{ij}, \vartheta^{\mathrm{R}}_{ij}, \varphi^{\mathrm{R}}_{ij}, \vartheta^{\mathrm{T}}_{\mathrm{M},ij}, \varphi^{\mathrm{T}}_{\mathrm{M},ij}, \vartheta^{\mathrm{R}}_{\mathrm{M},ij}, \varphi^{\mathrm{R}}_{\mathrm{M},ij}\right] \quad (2)$$

(a) The photo of the lab.

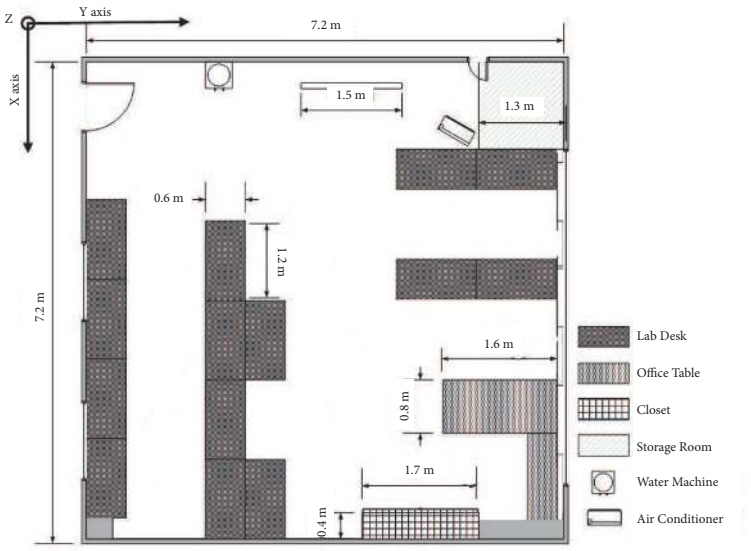

(b) The layout of the lab.

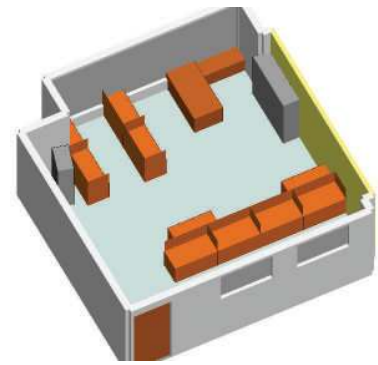

(c) The 3D ray tracing scenario of the lab.

Figure 3: The environment information of the lab scenario.

where ρ_{ij} is PL of the subchannel from i-th Tx antenna to j-th Rx antenna, $\mu_{ij}(\mu_{\mathrm{M},ij})$ is DS (DM) of the subchannel from i-th Tx antenna to j-th Rx antenna, $\vartheta^{\mathrm{T}}_{\mathrm{M},ij}$, $\vartheta^{\mathrm{R}}_{\mathrm{M},ij}$, $\vartheta^{\mathrm{T}}_{ij}$, and $\vartheta^{\mathrm{R}}_{ij}$ are AAMD, AAMA, AASD, and AASA, respectively, and $\varphi^{\mathrm{T}}_{\mathrm{M},ij}$, $\varphi^{\mathrm{R}}_{\mathrm{M},ij}$, $\varphi^{\mathrm{T}}_{ij}$, and $\varphi^{\mathrm{R}}_{ij}$ are EAMD, EAMA, EASD, and EASA, respectively. They can be further expressed as

$$\rho_{ij} = 10 \times \log_{10} \sum_{s=1}^{S} \alpha_{ij,s}^2 \tag{3}$$

$$\mu_{ij} = \sqrt{\frac{\sum_{s=1}^{S} \alpha_{ij,s}^2 \tau_{ij,s}^2}{\sum_{s=1}^{S} \alpha_{ij,s}^2} - \left(\frac{\sum_{s=1}^{S} \alpha_{ij,s}^2 \tau_{ij,s}}{\sum_{s=1}^{S} \alpha_{ij,s}^2} \right)^2} \tag{4}$$

$$\vartheta^{\mathrm{T}}_{ij} = \sqrt{\frac{\sum_{s=1}^{S} \alpha_{ij,s}^2 \theta^{\mathrm{T}}_{ij,s}{}^2}{\sum_{s=1}^{S} \alpha_{ij,s}^2} - \left(\frac{\sum_{s=1}^{S} \alpha_{ij,s}^2 \theta^{\mathrm{T}}_{ij,s}}{\sum_{s=1}^{S} \alpha_{ij,s}^2} \right)^2} \tag{5}$$

$$\vartheta^{\mathrm{R}}_{ij} = \sqrt{\frac{\sum_{s=1}^{S} \alpha_{ij,s}^2 \theta^{\mathrm{R}}_{ij,s}{}^2}{\sum_{s=1}^{S} \alpha_{ij,s}^2} - \left(\frac{\sum_{s=1}^{S} \alpha_{ij,s}^2 \theta^{\mathrm{R}}_{ij,s}}{\sum_{s=1}^{S} \alpha_{ij,s}^2} \right)^2} \tag{6}$$

$$\varphi^{\mathrm{T}}_{ij} = \sqrt{\frac{\sum_{s=1}^{S} \alpha_{ij,s}^2 \phi^{\mathrm{T}}_{ij,s}{}^2}{\sum_{s=1}^{S} \alpha_{ij,s}^2} - \left(\frac{\sum_{s=1}^{S} \alpha_{ij,s}^2 \phi^{\mathrm{T}}_{ij,s}}{\sum_{s=1}^{S} \alpha_{ij,s}^2} \right)^2} \tag{7}$$

$$\varphi^{\mathrm{R}}_{ij} = \sqrt{\frac{\sum_{s=1}^{S} \alpha_{ij,s}^2 \phi^{\mathrm{R}}_{ij,s}{}^2}{\sum_{s=1}^{S} \alpha_{ij,s}^2} - \left(\frac{\sum_{s=1}^{S} \alpha_{ij,s}^2 \phi^{\mathrm{R}}_{ij,s}}{\sum_{s=1}^{S} \alpha_{ij,s}^2} \right)^2} \tag{8}$$

$$\mu_{\mathrm{M},ij} = \frac{\sum_{s=1}^{S} \tau_{ij,s}}{S} \tag{9}$$

$$\vartheta^{\mathrm{T}}_{\mathrm{M},ij} = \frac{\sum_{s=1}^{S} \theta^{\mathrm{T}}_{ij,s}}{S} \tag{10}$$

$$\vartheta^{\mathrm{R}}_{\mathrm{M},ij} = \frac{\sum_{s=1}^{S} \theta^{\mathrm{R}}_{ij,s}}{S} \tag{11}$$

$$\varphi^{\mathrm{T}}_{\mathrm{M},ij} = \frac{\sum_{s=1}^{S} \phi^{\mathrm{T}}_{ij,s}}{S} \tag{12}$$

$$\varphi^{\mathrm{R}}_{\mathrm{M},ij} = \frac{\sum_{s=1}^{S} \phi^{\mathrm{R}}_{ij,s}}{S}. \tag{13}$$

After data preprocessing, the details of datasets are shown in Table 1. We separated the total samples into train sets and validation sets by the proportion of 7:3 randomly.

4. Architecture of the Proposed CNN for Channel Characteristics Prediction

The architecture of the CNN is presented in Figure 4. It includes two main stages: first stage configuring two convolutional layers and second stage configuring four dense layers which are also called fully connected layers. It requires a large number of iterations to obtain the neural network convergence to fit the thresholds nodes and the weights of connections for the least loss. The input vector X_{ij} is 3D coordinates of the i-th Tx antenna and the j-th Rx antenna. The output vector Y_{ij} is the channel characteristic vector of the subchannel between the i-th Tx and the j-th Rx ϖ_{ij}. They can be expressed as

$$X_{ij} = \left[x_{ij}^{\mathrm{T}}, y_{ij}^{\mathrm{T}}, z_{ij}^{\mathrm{T}}, x_{ij}^{\mathrm{R}}, y_{ij}^{\mathrm{R}}, z_{ij}^{\mathrm{R}}\right] \tag{14}$$

$$\begin{aligned} Y_{ij} &= \varpi_{ij} \\ &= \left[\rho_{ij}, \mu_{ij}, \mu_{\mathrm{M},ij}, \vartheta_{ij}^{\mathrm{T}}, \varphi_{ij}^{\mathrm{T}}, \vartheta_{ij}^{\mathrm{R}}, \varphi_{ij}^{\mathrm{R}}, \vartheta_{\mathrm{M},ij}^{\mathrm{T}}, \varphi_{\mathrm{M},ij}^{\mathrm{T}}, \vartheta_{\mathrm{M},ij}^{\mathrm{R}}, \varphi_{\mathrm{M},ij}^{\mathrm{R}}\right]. \end{aligned} \tag{15}$$

The first convolutional layer filters the 1×6 input vector with 16 kernels of size 1×3. The second convolutional layer takes the output of the first convolutional layer as input and filters it with 32 kernels of size 16×3. Both of the two convolutional layers take with a stride of one node. We zero pad the activation to match the number of features. After each convolutional layer, batch normalization in [48] and rectified linear unit (ReLU) are placed to speed up the model convergence. The output of the second convolutional layer is then fully connected to 16 neurons. The following dense layers have 16, 32, 64, and 1 neurons, respectively. In order to obtain the optimized training result, we train the 11 channel characteristics individually by the CNN. Each time we input all 6 elements of X_{ij} into CNN and output 1 element of Y_{ij}. ReLU is placed after each dense layer except the last layer. Unlike in computer vision, we do not place pooling layer between the convolutional layers, because the input of our network which is only 6 nodes is relatively sparser than the image which commonly contains millions of pixels. Pooling layer will lose useful information and make the model convergence at a high loss.

As shown in Table 2, this model has 7280 parameters in total. Most parameters are between the second convolutional layer and the first dense layer. The number of these parameters accounts for 42.20% of the total number of model parameters.

The CNN of one output node was designed. The 11 different labels (PL, DM, DS, AAMA, AASA, AAMD, AASD, EAMA, EASA, EAMD, and EASD) are individually used to train the CNN to obtain the different weights in terms of the least loss. Once the label is determined, the loss function and back propagation are applied end-to-end. The mean square error (MSE) function is used as the loss function in all CNNs of 11 labels. The learning rate is fixed throughout once training. We used an equal learning rate which was initialized at 0.0001 for all layers. The root mean square propagation (RMSProp) in [49] with momentum of 0.9 and smooth factor of 10^{-6} is used to optimize the weights of the model. The update rule for weight β is

$$E\left[g^2\right]_t = 0.9E\left[g^2\right]_{t-1} + 0.1g_t^2 \tag{16}$$

$$\beta_{t+1} = \beta_t - \frac{\eta}{\sqrt{E\left[g^2\right]_t + \kappa}} g_t \tag{17}$$

where t is the iteration index, η is the learning rate, κ is smooth factor, and g_t is the gradient of the current iteration t.

Glorot uniform initializer in [50], which is also called Xavier uniform initializer, was used to initialize the weights in each layer. The weight was randomly created from a uniform distribution within $[-\varepsilon, \varepsilon]$ with

$$\varepsilon = \sqrt{\frac{6}{\iota_{in} + \iota_{out}}} \tag{18}$$

where ι_{in} is the number of input units and ι_{out} is the number of output units in the weight tensor. We initialized the neuron biases in both convolutional layers and dense layers with the constant 0. This initialization accelerates the early stages of learning by providing the ReLUs with positive inputs.

5. Results and Analysis

The target of this section is twofold. The first intention is to verify the CNN in two indoor scenarios. Second, we will carry out comparisons between five different datasets to analyze the influence of dataset in CNN.

5.1. Fittings between Predicted and Real Channel Characteristics. In both the virtual classroom scenario and the lab scenario, all the predicted channel statistical characteristics generated by the CNN are in fairly good agreements with the channel statistical characteristics generated by the ray tracing software. In Figures 5–7, we show the fittings of PL, DM, and AAMA between predicted results and virtual simulation data in the two scenarios, respectively. As we can see, the predicted capability of the CNN is very good, and we can use this method to predict the channel statistical characteristics with limited simulation data in specified indoor scenarios. This shows that AI is meaningful for channel modeling. The massive data in wireless communication should be fully used and explored to make the performance of wireless communication networks better.

5.2. RMSE. To evaluate and compare the performances of the CNN with different datasets, we calculate the RMSE between predicted channel statistical characteristics and virtual simulation channel statistical characteristics; i.e.,

$$R(l) = \sqrt{\mathrm{E}\left[\left(l_p - l_r\right)^2\right]} \tag{19}$$

Table 1: The Details of Databases.

Scenario	Dataset	Tx	Rx	No. of sample	No. of train set	No. of validation set
Virtual scenario	10100R	10	100	1000	700	300
	3232R	32	32	1024	717	307
Lab scenario	3030R	30	30	900	630	270
	3030G	30	30	900	630	270
	211211G	211	211	44521	31165	13356

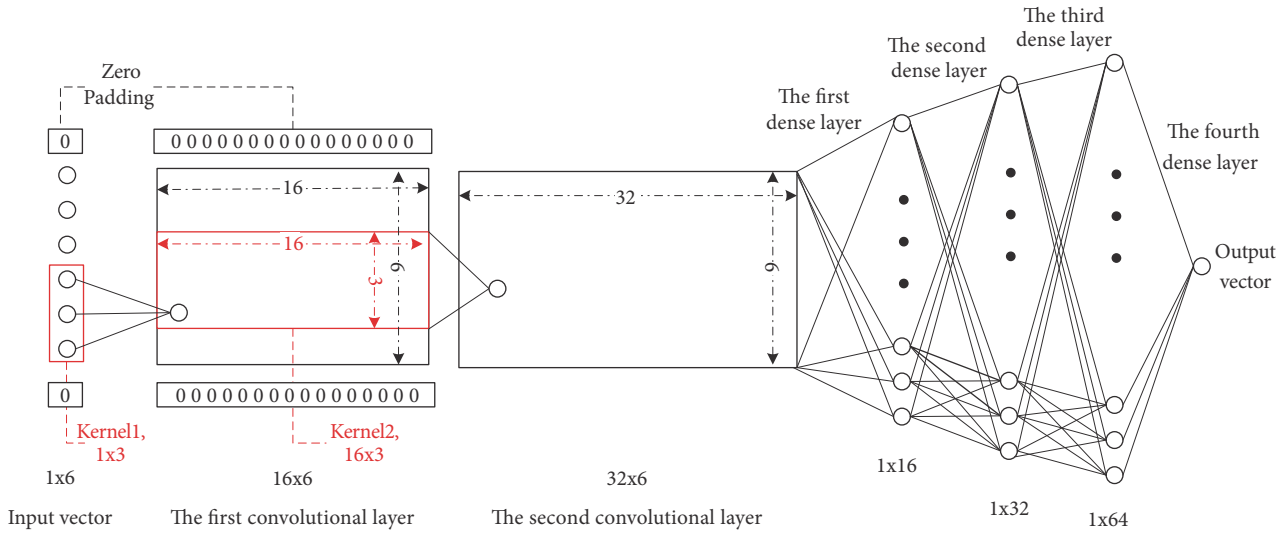

Figure 4: Architecture of the proposed CNN for channel statistical characteristics prediction.

Table 2: The parameter numbers of CNN layers.

Layers	No. of parameters
First convolutional layer	48
Second convolutional layer	1536
First dense layer	3072
Second dense layer	512
Third dense layer	2048
Fourth dense layer	64
Total	7280

where $R(l)$ is the RMSE of the channel characteristic l, such as PL, DM, DS, AAMA, AASA, AAMD, AASD, EAMA, EASA, EAMD, and EASD. l_p and l_r denote the predicted result and virtual simulation result of the channel characteristic, respectively.

The RMSEs of channel statistical characteristics with two datasets in the virtual scenario are listed in Table 3. Train loss (TL) is the RMSE between the channel characteristic generated by the CNN and the virtual simulation channel characteristic in train data. Validation loss (VL) is the RMSE between the channel characteristic predicted by the CNN and the virtual measurement channel characteristic in the test data. In Table 3, VL of channel statistical characteristics of the 10100R is always larger than TL. Similar result is shown in the 3232R. The parameters of the CNN are trained based on MSE optimizer in the train data, and the test data is different for the train data absolutely. So the results in the test data cannot be optimized as good as those in the train data. The performance of the CNN in the 10100R is better than in the 3232R, which is most obvious in the PL. The TL of the PL in 10100R (0.6408) is only 14.26% of that in 3232R (4.4932). The VL of the PL in 10100R (0.9586) is only 20.04% of that in 3232R (4.7832).

The RMSEs of channel statistical characteristics with two datasets in the lab scenario are listed in Table 4. As we can see, the performance of the CNN in the 3030G is better than that in the 3030R, which is most obvious in the PL. The TL of the PL in 3030G (1.0616) is only 34.70% of that in 3030R (3.0590). The VL of the PL in 3030G (1.3186) is only 41.27% of that in 3030R (3.1949). The performance of the CNN in the 211211G is better than that in the 3030G, which is most obvious in the AAMD. The TL of the AAMD in 211211G (6.7187) is only 47.27% of that in 3030G (14.2148). The VL of the AAMD in 211211G (7.1652) is only 35.24% of that in 3030G (20.3331).

There are 1024 samples and 1000 samples in the 3232R and the 10100R, respectively. The sample numbers of the two datasets belong to the same order of magnitudes, and both of them are generated when Txs and Rxs are randomly located. According to the specified Tx antenna locations, there are 100 samples with different Rx antenna locations in the 10100R, while there are only 32 samples with different Rx antenna locations in the 3232R. The former is more various and more robust, which explains that the performance of 10100R is better than 3232R. The performance is determined by the robustness of data even they are in the same order

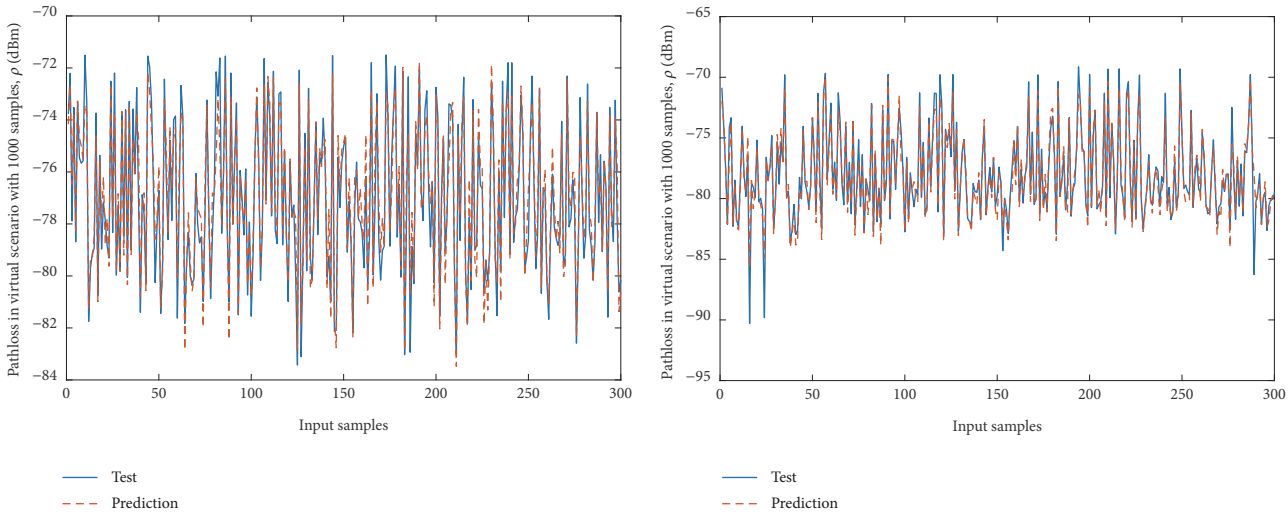

(a) In the virtual scenario. (b) In the lab scenario.

Figure 5: The predicted fitting of PL in two scenarios.

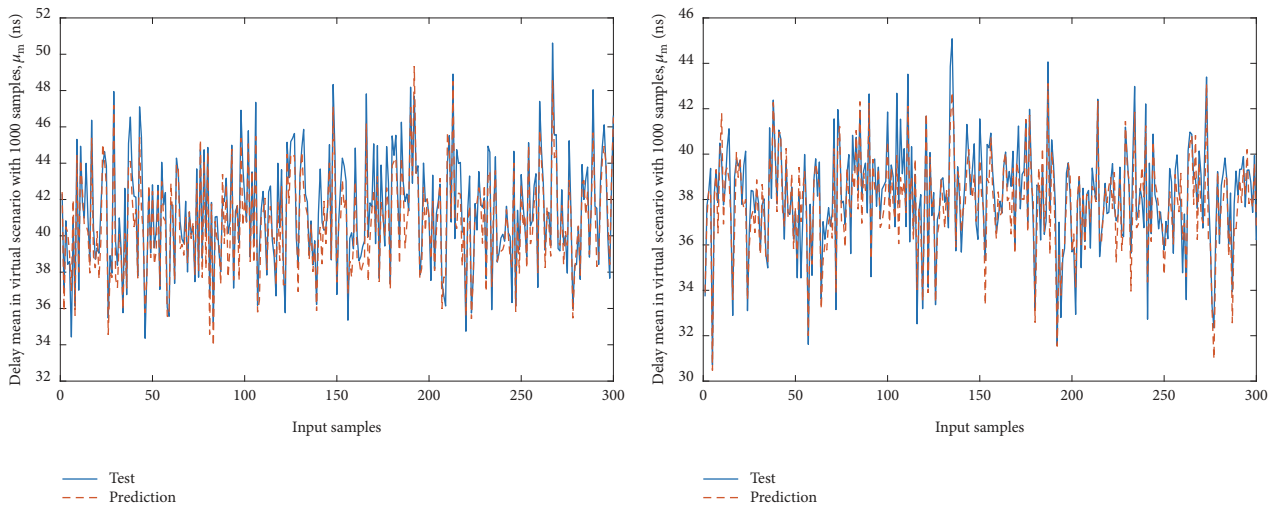

(a) In the virtual scenario (b) In the lab scenario

Figure 6: The predicted fitting of DM in two scenarios.

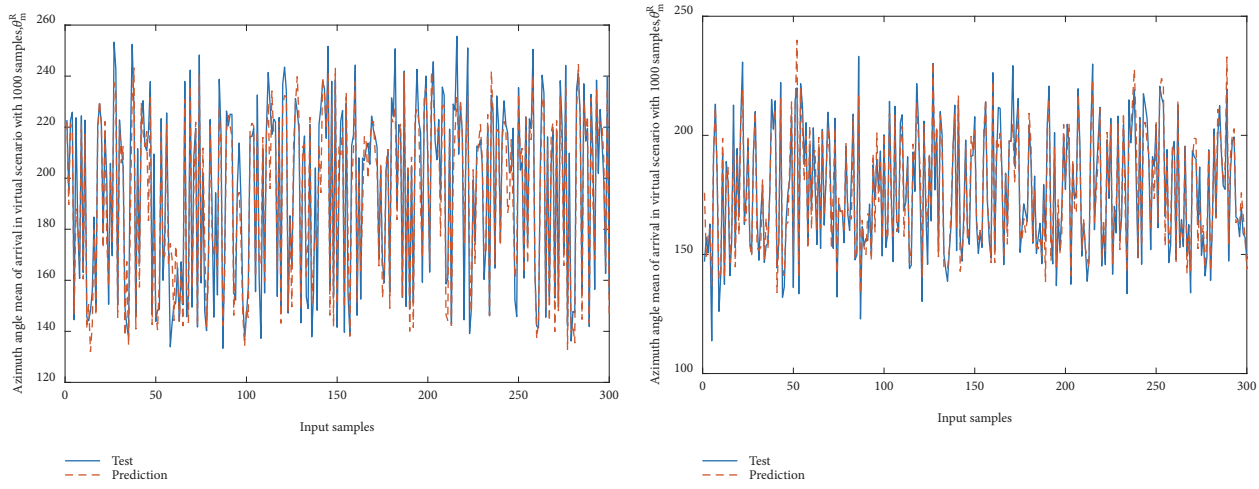

(a) In the virtual scenario (b) In the lab scenario

Figure 7: The predicted fitting of AAM in two scenarios.

Table 3: RMSE Loss with Different Dataset in the Virtual Scenarios.

Dataset	10100R		3232R		10100R and 3232R	
RMSE	TL	VL	TL	VL	TL in 10100R / TL in 3232R	VL in 10100R / VL in 3232R
PL	0.6408	0.9586	4.4932	4.7832	0.1426	0.2004
DM	0.4232	0.4762	1.2986	2.3647	0.3259	0.2014
DS	0.2895	0.3708	1.7822	1.9887	0.1624	0.1865
AAMA	11.0096	13.3897	14.3276	14.4829	0.7684	0.9245
AASA	4.6625	5.6897	17.2259	18.7624	0.2707	0.3033
AAMD	11.8287	13.4187	12.8583	14.6427	0.9199	0.9164
AASD	5.3249	6.3327	21.0490	21.3898	0.2529	0.2961
EAMA	1.3355	1.4970	3.8356	4.8577	0.3482	0.3082
EASA	1.5680	1.8255	3.5929	3.8308	0.4364	0.4765
EAMD	0.8228	0.9298	2.8473	4.3977	0.2890	0.2114
EASD	2.3911	3.0512	2.7861	3.2362	0.8582	0.9428

Table 4: RMSE Loss with Different Dataset in the Lab Scenarios.

Dataset	3030R		3030G		211211G		3030G and 3030R		211211G and 3030G	
RMSE	TL	VL	TL	VL	TL	VL	TL in 3030G / TL in 3030R	VL in 3030G / VL in 3030R	TL in 211211G / TL in 3030G	VL in 211211G / VL in 3030G
PL	3.0596	3.1949	1.0616	1.3186	1.0439	1.1459	0.3470	0.4127	0.9833	0.8690
DM	1.8142	2.0642	1.4970	1.8566	1.0196	1.0645	0.8252	0.8994	0.6811	0.5734
DS	0.4866	0.5037	0.2698	0.3528	0.2168	0.3038	0.5545	0.7004	0.8036	0.8611
AAMA	19.1869	19.8408	8.9489	9.0166	7.0688	7.5453	0.4664	0.4544	0.7899	0.8368
AASA	12.6992	12.2539	8.0887	8.4545	5.1746	5.8588	0.6369	0.6899	0.6397	0.6930
AAMD	17.7100	20.5364	14.2148	20.3331	6.7187	7.1652	0.8026	0.9901	0.4727	0.3524
AASD	15.1566	14.7420	8.3635	12.6681	6.2428	6.5880	0.5518	0.8593	0.7464	0.5200
EAMA	3.3544	3.4216	1.4747	1.7197	1.2807	1.4928	0.4396	0.5026	0.8684	0.8681
EASA	1.5093	1.8472	0.8160	0.6658	0.8084	0.4824	0.5356	0.3604	0.9907	0.7245
EAMD	2.2215	2.4836	1.9990	1.9906	1.6045	1.7258	0.8998	0.8015	0.8027	0.8670
EASD	0.3008	0.3739	0.2989	0.3697	0.2287	0.2360	0.9937	0.9888	0.7603	0.6384

of magnitudes. It is determined by the robustness of data. The comparison between the performance of 3030G and 3030R shows that the data collection in grid is better than that in random. The comparison between the performance of 211211G and 3030G shows that more robust data generated by the specified collection way results in a better predicted performance. The above-mentioned conclusions have significant meaning on data collection.

5.3. PDF of Channel Characteristics Error Square. For the further analysis of the performance of five different datasets, the PDF of channel statistical characteristics error square which can show the distribution of the channel statistical characteristics error square are given in Figure 8. The PDFs of error square of DM and AAMA are shown in Figures 8(a) and 8(b), respectively. In view of that the train loss and validation loss in the 211211G of lab scenario are only slightly lower than those of the 3030G in lab scenario in Table 4, and the advantage of large dataset is not obvious if we take the time and energy consuming of data collection into account. However, Figures 8(a) and 8(b) show that the core superiority of the 211211G in lab scenario is the PDFs of error square in which the proportion of accurate predicted channel characteristic (error square = 0) is very large. It is better that the lower channel characteristic error square has higher probability and vice versa. In Figure 8(b), the proportion of accurate predicted AAMA of the 3232R in the virtual scenario (error square = 0) is larger than that of the 10100R in the virtual scenario, but the proportion of predicted AAMA with a high error square in the 3232R in the virtual scenario is also larger than that of the 10100R in the virtual classroom scenario. The fleet decline tendency of PDF of channel characteristic error square is what we expected.

6. Conclusions and Future Work

The AI enabled procedure to predict channel statistical characteristics has been proposed in this paper. The channel parameters of massive MIMO and mmWave indoor channel have been generated by a ray tracing software Wireless InSite. The channel statistical characteristics after data preprocessing, such as PL, DM, DS, AAMA, AASA, AAMD, AASD, EAMA, EASA, EAMD, and EASD, can be predicted by CNN. A virtual classroom scenario and a real lab scenario

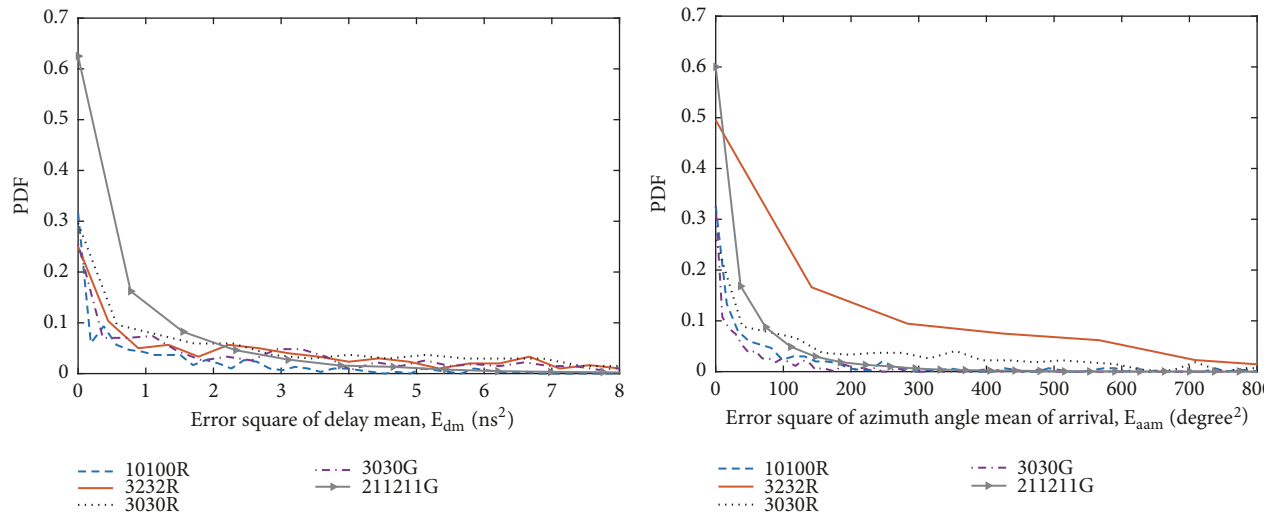

(a) The PDF of DM error square.

(b) The PDF of AAMA error square.

FIGURE 8: The PDF of channel statistical characteristics error square with different datasets.

have been set up to verify this algorithm. The good fittings between the predicted channel statistical characteristics and the real channel statistical characteristics have been shown in this paper. By comparing between the performance of different datasets, the better data collection rule has also been proposed. The generalization of AI enabled procedure to predict channel statistical characteristics for more scenarios is an important task to be solved in the future.

Data Availability

The data can be made available if requested.

Conflicts of Interest

The authors declare that there are no conflicts of interest regarding the publication of this paper.

Acknowledgments

The authors gratefully acknowledge the support from the National Natural Science Foundation of China (no. 61771293), the Science and Technology Project of Guangzhou (no. 201704030105), the EPSRC TOUCAN project (no. EP/L020009/1), the EU H2020 5G Wireless project (no. 641985), the EU H2020 RISE TESTBED project (no. 734325), the Key R&D Program of Shandong Province (no. 2016GGX101014), the Fundamental Research Funds of Shandong University (no. 2017JC029), and the Taishan Scholar Program of Shandong Province.

References

[1] J. G. Andrews, S. Buzzi, W. Choi et al., "What will 5G be?" *IEEE Journal on Selected Areas in Communications*, vol. 32, no. 6, pp. 1065–1082, 2014.

[2] Huawei, "5G a technology vision," White Paper, https://www.huawei.com/ilink/en/download/HW_314849.

[3] Samsung, "5G vision," White Paper, https://www.samsung.com/global/business/networks/insights/5g-vision/.

[4] I. Gaspar and G. Wunder, "5G cellular communications scenarios and system requirements," Tech. Rep., 2013, https://www.5gnow.eu/.

[5] C.-X. Wang, F. Haider, X. Gao et al., "Cellular architecture and key technologies for 5G wireless communication networks," *IEEE Communications Magazine*, vol. 52, no. 2, pp. 122–130, 2014.

[6] X. Ge, S. Tu, G. Mao, C.-X. Wang, and T. Han, "5G ultra-dense cellular networks," *IEEE Wireless Communications Magazine*, vol. 23, no. 1, pp. 72–79, 2016.

[7] A. Molish, *Wireless Communications*, John Wiley & Sons, London, UK, 2011.

[8] V. Nurmela, A. Karttunen, A. Roivainen et al., "METIS channel models," METIS ICT-317669/D1.4, 2015.

[9] A. Maltsev, A. Pudeyev, I. Bolotin et al., "Channel modeling and characterization," MiWEBA FP7-ICT-608637/D5.1, V1.0, 2014.

[10] ITU-R, "Preliminary draft new report ITU-R M. [IMT-2020.EVAL]," Tech. Rep. R15-WP5D-170613-TD-0332, ITU-R, Niagara Falls, Canada, 2017.

[11] L. Liu, C. Oestges, J. Poutanen et al., "The COST 2100 MIMO channel model," *IEEE Wireless Communications Magazine*, vol. 19, no. 6, pp. 92–98, 2012.

[12] R. Verdone and A. Zanella, *Pervasive Mobile and Ambient Wireless Communications*, Springer, London, UK, 2012.

[13] A. Maltsev, A. Pudeyev, A. Lomayev, and I. Bolotin, "Channel models for IEEE 802.11ay," IEEE doc 802.11-15/1150r9, 2016.

[14] mmMAGIC, "Millimetre-Wave Based Mobile Radio Access Network for Fifth Generation Integrated Communications," mmMAGIC H2020-ICT-671650-mmMAGIC/D2.1, v1.0, 2016.

[15] A. Maltsev, A. Pudeyev, I. Karls et al., "Quasi-deterministic approach to mmWave channel modeling in a non-stationary environment," in *Proceedings of the IEEE Globecom Workshops (GC Wkshps '14)*, pp. 966–971, Austin, Tex, USA, December 2014.

[16] S. Jaeckel, L. Raschkowski, K. Borner, and L. Thiele, "QuaDRiGa: a 3-D multi-cell channel model with time evolution for enabling virtual field trials," *IEEE Transactions on Antennas and Propagation*, vol. 62, no. 6, pp. 3242–3256, 2014.

[17] S. Wu, C.-X. Wang, H. Aggoune, M. M. Alwakeel, and X. You, "A general 3-D non-stationary 5G wireless channel model," *IEEE Transactions on Communications*, vol. 66, no. 7, pp. 3065–3078, 2018.

[18] J. Huang, C.-X. Wang, R. Feng, J. Sun, W. Zhang, and Y. Yang, "Multi-Frequency mmWave Massive MIMO Channel Measurements and Characterization for 5G Wireless Communication Systems," *IEEE Journal on Selected Areas in Communications*, vol. 35, no. 7, pp. 1591–1605, 2017.

[19] R. Feng, J. Huang, J. Sun, and C. Wang, "A novel 3D frequency domain SAGE algorithm with applications to parameter estimation in mmWave massive MIMO indoor channels," *Science China Information Sciences*, vol. 60, no. 8, 2017.

[20] C.-X. Wang, S. Wu, L. Bai, X. You, J. Wang, and C.-L. I, "Recent advances and future challenges for massive MIMO channel measurements and models," *Science China Information Sciences*, vol. 59, no. 2, pp. 1–16, 2016.

[21] P. Ferrand, M. Amara, S. Valentin, and M. Guillaud, "Trends and challenges in wireless channel modeling for evolving radio access," *IEEE Communications Magazine*, vol. 54, no. 7, pp. 93–99, 2016.

[22] S. Bi, R. Zhang, Z. Ding, and S. Cui, "Wireless communications in the era of big data," *IEEE Communications Magazine*, vol. 53, no. 10, pp. 190–199, 2015.

[23] L. O. Chua and T. Roska, "CNN paradigm," *IEEE Transactions on Circuits and Systems I: Fundamental Theory and Applications*, vol. 40, no. 3, pp. 147–156, 1993.

[24] R. He, Q. Li, B. Ai et al., "An automatic clustering algorithm for multipath components based on kernel-power-density," in *Proceedings of the IEEE Wireless Communications and Networking Conference (WCNC '17)*, pp. 1–6, San Francisco, Calif, USA, March 2017.

[25] R. He, Q. Li, B. Ai et al., "A kernel-power-density-based algorithm for channel multipath components clustering," *IEEE Transactions on Wireless Communications*, vol. 16, no. 11, pp. 7138–7151, 2017.

[26] C. Huang, R. He, Z. Zhong, Y.-A. Geng, Q. Li, and Z. Zhong, "A Novel Tracking-Based Multipath Component Clustering Algorithm," *IEEE Antennas and Wireless Propagation Letters*, vol. 16, pp. 2679–2683, 2017.

[27] N. Czink, R. Tian, S. Wyne et al., "Tracking Time-Variant Cluster Parameters in MIMO Channel Measurements," in *Proceedings of the 2nd IEEE International Conference on Communications and Networking in China (CHINA–COM '07)*, pp. 1147–1151, Shanghai, China, August 2007.

[28] N. Czink, P. Cera, J. Salo, E. Bonek, J.-P. Nuutinen, and J. Ylitalo, "A framework for automatic clustering of parametric MIMO channel data including path powers," in *Proceedings of the IEEE 64th Vehicular Technology Conference (VTC-Fall '06)*, pp. 1–5, Montreal, Canada, September 2006.

[29] N. Czink, P. Cera, J. Salo, E. Bonek, J.-P. Nuutinen, and J. Ylitalo, "Automatic clustering of MIMO channel parameters using the multipath component distance measure," in *Proceedings of the International Symposium on Wireless Personal Multimedia Communications (WPMC '05)*, 2005.

[30] N. Zaarour, N. Kandil, and N. Hakem, "An accurate neural network approach in modeling an UWB channel in an underground mine," in *Proceedings of the IEEE Antennas and Propagation Society International Symposium (APSURSI '13)*, pp. 1608-1609, Orlando, Fla, USA, July 2013.

[31] N. Zaarour, N. Kandil, N. Hakem, and C. Despins, "Comparative experimental study on modeling the path loss of an UWB channel in a mine environment using MLP and RBF neural networks," in *Proceedings of the 3rd International Conference on Wireless Communications in Underground and Confined Areas (ICWCUCA '12)*, Clermont Ferrand, France, August 2012.

[32] N. Zaarour, S. Affes, N. Kandil, and N. Hakem, "Comparative study on a 60 GHz path loss channel modeling in a mine environment using neural networks," in *Proceedings of the IEEE International Conference on Ubiquitous Wireless Broadband (ICUWB '15)*, Montreal, Canada, October 2015.

[33] M. Kalakh, N. Kandil, and N. Hakem, "Neural networks model of an UWB channel path loss in a mine environment," in *Proceedings of the IEEE 75th Vehicular Technology Conference (VTC Spring '12)*, Yokohama, Japan, June 2012.

[34] J. Huang, C.-X. Wang, L. Bai et al., "A big data enabled channel model for 5G wireless communication systems," *IEEE Transactions on Big Data*, In press.

[35] T. Moazzeni, "A wireless propagation channel model with meteorological quantities using neural networks," in *Proceedings of the IEEE GCC Conference (GCC '06)*, pp. 1–4, Manama, Bahrain, March 2006.

[36] Y. Ma, K. Liu, and Y. Guo, "Artificial neural network modeling approach to power-line communication multipath channel," in *Proceedings of the IEEE International Conference Neural Networks & Signal Processing*, Zhenjiang, China, June 2008.

[37] L. Lv, "A novel wireless channel model with multiply feedforward neural network," in *Proceedings of the 3rd International Conference on Natural Computation (ICNC '07)*, pp. 730–734, Haikou, China, August 2007.

[38] X. Ye, X. Yin, X. Cai, A. Perez Yuste, and H. Xu, "Neural-network-assisted UE localization using radio-channel fingerprints in LTE networks," *IEEE Access*, vol. 5, no. 5, pp. 12071–12087, 2017.

[39] X. Wang, L. Gao, S. Mao, and S. Pandey, "DeepFi: deep learning for indoor fingerprinting using channel state information," in *Proceedings of the IEEE Wireless Communications and Networking Conference (WCNC '15)*, pp. 1666–1671, New Orleans, La, USA, March 2015.

[40] M. Kotol and Z. Raida, "Comparison of neural models of UWB and 60 GHz in-car transmission channels," in *Proceedings of the International Conference on Broadband Communications for Next Generation Networks and Multimedia Applications (CoBCom '16)*, pp. 1–4, Graz, Austria, September 2016.

[41] M. Kotol, Z. Raida, and J. Velim, "Neural modeling of in-vehicle wireless channels: Wave propagation along the vehicle body at 60 GHz," in *Proceedings of the IEEE-APS Topical Conference on Antennas and Propagation in Wireless Communications (APWC '15)*, pp. 279–282, Turin, Italy, September 2015.

[42] J. Zhang, "The interdisciplinary research of big data and wireless channel: a cluster-nuclei based channel model," *China Communications*, vol. 13, Article ID 7833457, pp. 14–26, 2016.

[43] Wireless InSite Propagation Software, https://www.remcom.com/wireless-insite-em-propagation-software.

[44] ITU-R, "Effects of building materials and structures on radiowave propagation above about 100 MHz," ITU-R P.2040-1, 2015.

[45] J. Lu, D. Steinbach, P. Cabrol, P. Pietraski, and R. V. Pragada, "Propagation characterization of an office building in the 60

GHz band," in *Proceedings of the 8th European Conference on Antennas and Propagation (EuCAP '14)*, pp. 809–813, The Hague, Netherlands, April 2014.

[46] D. Ferreira, I. Cuinas, R. F. Caldeirinha, and T. R. Fernandes, "A review on the electromagnetic characterisation of building materials at micro- and millimetre wave frequencies," in *Proceedings of the 8th European Conference on Antennas and Propagation (EuCAP '14)*, pp. 145–149, The Hague, Netherlands, April 2014.

[47] K. Korolev and M. Afsar, "Complex dielectric permittivity measurements of materials in millimeter waves," in *Proceedings of the Joint 30th International Conference on Infrared and Millimeter Waves (IRMMW-THz '05)*, pp. 594-595, Williamsburg, Va, USA, September 2005.

[48] S. Ioffe and C. Szegedy, "Batch normalization: Accelerating deep network training by reducing internal covariate shift," https://arxiv.org/abs/1502.03167.

[49] Keras Document, https://keras.io/.

[50] X. Glorot and Y. Bengio, "Understanding the difficulty of training deep feedforward neural networks," *Journal of Machine Learning Research*, vol. 9, pp. 249–256, 2010.

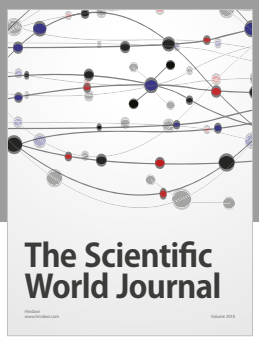

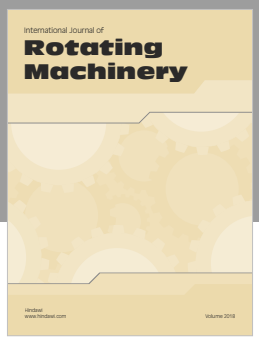

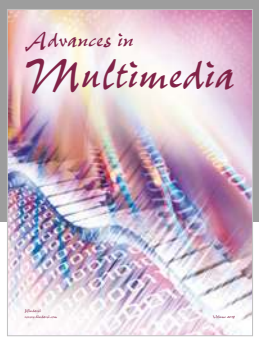

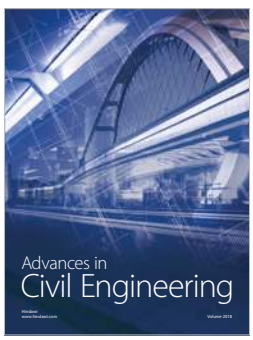


Hindawi
Submit your manuscripts at
www.hindawi.com